Magnetic and structural properties of amorphous CoTi soft ferromagnetic thin films. II. Structural properties

F. Machizaud,* K. Ounadjela,† and G. Suran
Laboratoire de Magnétisme, Centre National de la Recherche Scientifique, 92195 Meudon CEDEX, France
(Received 18 April 1988; revised manuscript received 3 October 1988)

The structure of amorphous $Co_{1-x}Ti_x$ thin films prepared by rf sputtering was studied by electron microscopy as a function of the deposition parameters and the concentration of the layers. We tried to simulate the experimental diffraction spectra by a structural model which took into account the short-range order observed in the corresponding crystalline alloy. The model which gave the best agreement with the experimental results is a random continuous network built up of clusters with trigonal, octahedral, and icosahedral symmetry. The size and the structural correlations between the various clusters were also determined. By changing the respective amount of the clusters we could simulate the slight variations of the characteristics of the diffused intensities obtained on samples deposited under a different pressure of the sputtering gas P_{Ar}. This structural model provided an explanation of the variations of the induced anisotropy K_u with P_{Ar} with thermomagnetic annealing, and as a function of the concentration of the films. These results are reported in paper I.

I. INTRODUCTION

The magnetic properties of amorphous $Co_{1-x}Ti_x$ thin films obtained by rf sputtering have been reported previously.[1,2] A detailed experimental study revealed that when the deposition process is performed in the presence of a magnetic field the magnitude of the induced in-plane uniaxial anisotropy K_u for a given concentration is mainly related to the pressure of the sputtering gas P_{Ar}. The large value of K_u and the as-observed variations with P_{Ar} could not be explained by the usually proposed mechanism related to a directional short-range order.[3–5] Consequently we developed a new model where these results are related to the particular local structure of Co-rich $Co_{1-x}Ti_x$ amorpous thin films and to the evolution of the local structure with P_{Ar}.[2]

We report hereafter the detailed structural study performed on the $Co_{1-x}Ti_x$ thin films using electron microscope techniques and the as-proposed structural model. The model established permitted us to simulate by computer calculation the scattered intensity deduced from the experimental transmission electron diffraction data, and to explain the variations of K_u with P_{Ar} and the concentration x of the films.

II. EXPERIMENTAL DETAILS

The $Co_{1-x}Ti_x$ films were deposited by rf diode sputtering. During the deposition a magnetic field was applied parallel to the substrate. The details of the preparation process are given in the first part of this paper. For structural studies 400 to 600 Å thick films were deposited onto carbon-coated electron microscope grids.

The dependence upon the concentration of the structure and morphology was studied for the range $0.09 \leq x \leq 0.22$. Here we report results obtained on four sets of samples called A ($x=0.09$), B ($x=0.12$), C ($x=0.14$), and D ($x=0.22$). The structural changes as a function of P_{Ar} were investigated on samples deposited at $P_{Ar}=3$ mTorr (films $A3$, $B3$, $C3$), 15 mTorr (films $A15$, $B15$, $C15$), and 8 mTorr (films $A8$, $B8$, $C8$, $D8$). These values of P_{Ar} were chosen following the magnetic properties of the samples. They correspond, respectively, to the lowest and highest deposition pressure used and to the value of P_{Ar} for which $(K_u)_{max}$ is obtained.[2] The morphology of the layers were studied by high-resolution transmission electron micrographs (TEM) and the structure deduced from transmission electron diffraction patterns (TEDP).

III. STRUCTURAL STUDIES

The structure of an amorphous alloy is characterized by its local atomic ordering. It was frequently observed that this short-range atomic order (SRO) exhibits similarities with the local symmetry of the corresponding crystalline compound. Therefore we extended our structural investigations to samples A and B which in the as-deposited state are microcrystalline and to amorphous C alloys annealed at temperatures higher than the crystallization temperature.

A. Transmission electron micrographs (TEM)

The TEM obtained in bright and dark fields (first diffused ring paraxial) confirmed the structural homogeneity of the films having the highest Ti concentration. On samples $C3$, $C8$, $C15$, and $D8$ the dark-field micrographs present the "salt and pepper" feature characteristic of an amorphous alloy and no microcrystallite could be detected (Fig. 1). On all these samples the TEM exhibits a weak contrast, the largest discernable detail being smaller than 10 Å. Nevertheless the effect of P_{Ar} upon the morphology of films C could be clearly observed, as the TEM corresponding to samples deposited at higher

pressures are more contrasted. One observes some kind of boundaries which are thinner and better resolved when P_{Ar} is higher (samples $C8$ and $C15$) but unobservable on sample $C3$. The same kind of contrast was observed also in the amorphous matrix of the partially crystallized samples $B8$ and $B15$ (Fig. 2). This microstructure could indicate some fluctuation of the local composition and/or of the density. Such fluctuations were effectively detected by small-angle scattering on thin films deposited by sputtering, while they were not observed when the same compounds were obtained in an amorphous state by quenching of the melt.[6] The sample $B3$ deposited at low P_{Ar} appears to be amorphous (Fig. 2). In films $B8$ and $B15$ which were deposited at higher pressure and are partially amorphous, the number of microscrystallites increases with increasing P_{Ar}. By contrast samples of series A which have the lowest Ti content are microcrystalline for all P_{Ar}. In sample $A3$ the microcrystallites are disseminated in an amorphous matrix as result of low P_{Ar} used. These observations show clearly that the use of a low P_{Ar} during the deposition process favors the obtention of the amorphous state.

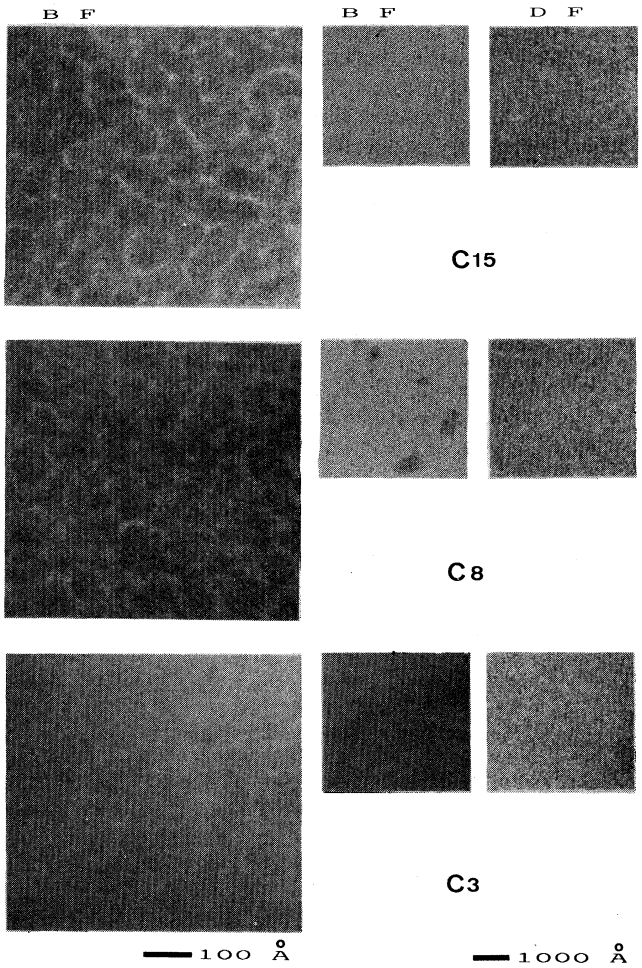

FIG. 1. Microstructure of $Co_{86}Ti_{14}$ thin films in bright field (BF) and dark field (DF) and evolution with P_{Ar}. Samples $C3$, $C8$, and $C15$ were deposited, respectively, at 3, 8, and 15 mTorr.

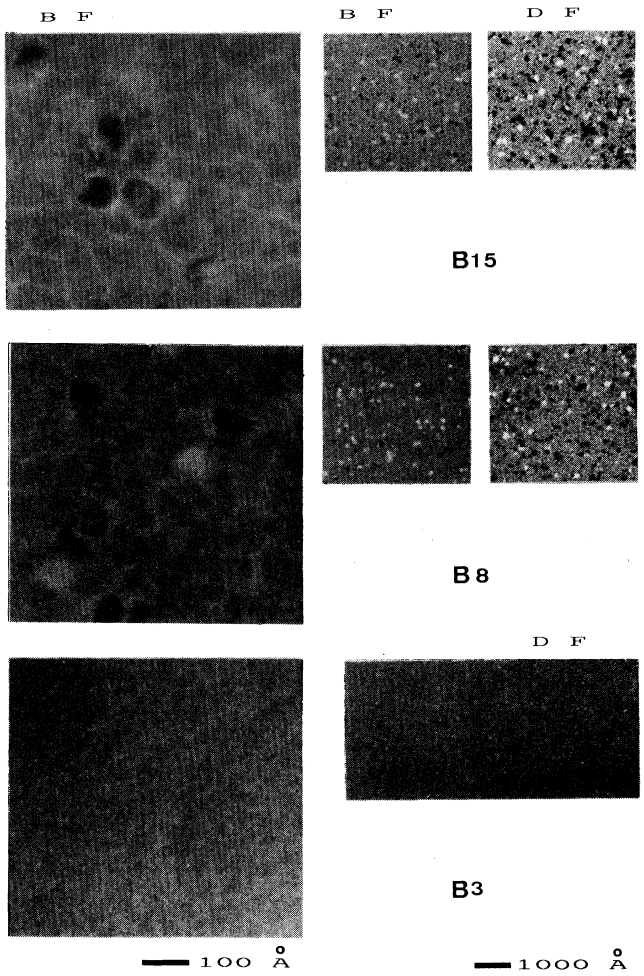

FIG. 2. Microstructure of $Co_{88}Ti_{12}$ thin films in BF and DF samples $B3$, $B8$, and $B15$ were deposited, respectively, at $P_{Ar}=3$, 8, and 15 mTorr.

B. Transmission electron diffraction patterns (TEDP)

The TEDP's were realized on photographic films without energy analysis. They exhibit both elastic and inelastic contributions. The electron diffraction patterns were traced from the photographic films by a microdensitometer and resolved up to $s=2\sin\theta/\lambda=1.4$ Å^{-1}, where s is the scattering vector.

The characteristics of the diffraction patterns agree with observations obtained by TEM. The patterns corresponding to samples $B3$, $C3$, $C8$, $C15$, and $D8$ exhibit characteristics typical of the amorphous state (Figs. 3 and 4): One observes three broad and diffused halos without contamination of the Bragg peaks since the TEM's in dark field do not reveal microcrystallites. The second

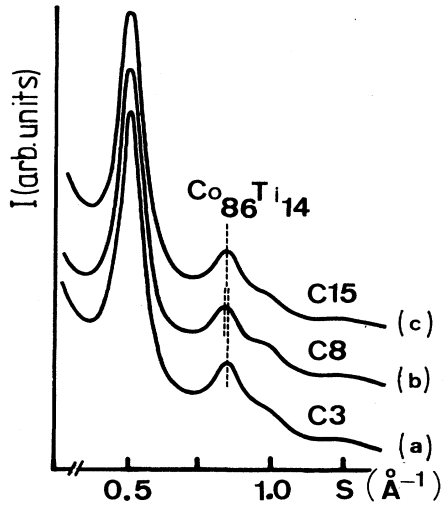

FIG. 3. TEDP profile of $Co_{86}Ti_{14}$ films. (a) $P_{Ar}=3$ mTorr, (b) $P_{Ar}=8$ mTorr, and (c) $P_{Ar}=15$ mTorr.

halo at $s\approx 0.85$ Å^{-1} is split. The effect of P_{Ar} is reported in Fig. 3. On samples $C8$ an $C15$ the maximum corresponding to the second halo shift toward lower values of s. This shift is the highest for sample $C8$ that exhibits the more contrasted shoulder. Since the accuracy of structural study by electron microdiffraction is rather limited, we cross checked and confirmed these results by investigating three different sets of samples C and performed the measurements on four different microscopes. All these observations were fairly well reproducible so we can consider them as being really significant. The variations with concentration are illustrated in Fig. 4. With increasing Ti concentration the shoulder on the second peak is progressively attenuated. Although this change as a function of concentration appears to be slight, it is of the same order of magnitude as those observe, for instance, in bulk amorphous $Cu_{1-x}Ti_x$ alloys.[10] On these compounds the same type of variation was observed by x-ray diffraction but for a larger range of compositions $(0.30\leq x\leq 0.65)$.

Samples $A3$, $B8$, and $B15$ exhibit a partially microcrystalline structure. The corresponding diffraction pattern consists of the superimposed broad halos and weak Bragg lines. Films $A8$ and $A15$ possess a microcrystalline structure which is a mixture of the hcp and fcc phases (Figs. 4 and 5). The respective amount of the phases is strongly related to the value of the P_{Ar} used. The hcp character is favored by the high P_{Ar}: All the lines $(hkjl)$ corresponding to the hcp phase are clearly detected on the TEDP's which correspond to samples $A8$ and $A15$ while there is a tendency towards the formation of an fcc structure at the lowest P_{Ar} as observed on sample $A3$. The first peak at $s=0.5$ Å^{-1} becomes more intense and extends asymetrically at the higher values of s; this result corresponds, respectively, to an increase of the intensity of the (111) and the (200) lines.

Annealing of samples $C3$ and $C8$ just above the crystallization temperature ($T_c\geq 400$ °C) confirmed the predominance of the hcp or fcc symmetry which must exist initially in the amorphous state and is also related to the value of P_{Ar}. The hcp character is favored by the use of a high P_{Ar} as shown clearly on the TEDP profile cor-

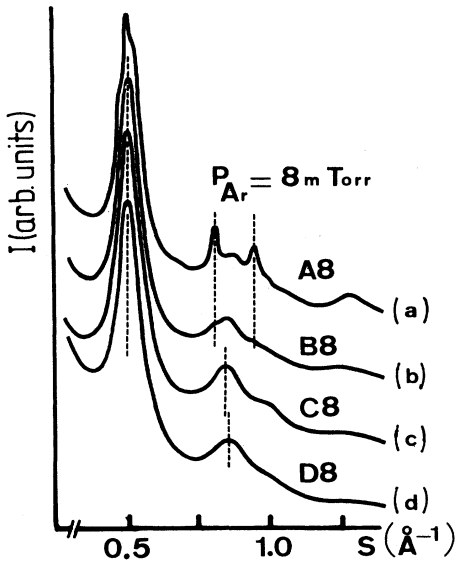

FIG. 4. Variation of the TEDP profile on $Co_{1-x}Ti_x$ thin films with Ti concentration for samples deposited at $P_{Ar}=8$ mTorr: (a) $x=0.09$, (b) $x=0.12$, (c) $x=0.14$, and (d) $x=0.22$.

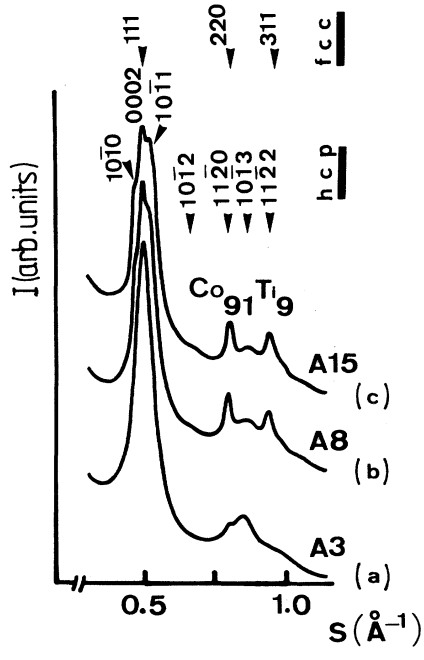

FIG. 5. TEDP profile of $Co_{91}Ti_9$ films (A series). (a) $P_{Ar}=3$ mTorr, (b) $P_{Ar}=8$ mTorr, and (c) $P_{Ar}=15$ mTorr.

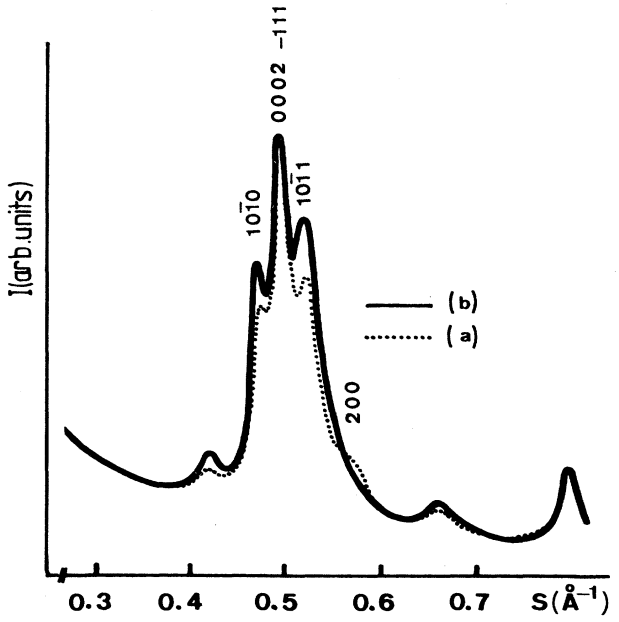

FIG. 6. TEDP profiles of $Co_{86}Ti_{14}$ films annealed at 400 °C. (a) $P_{Ar}=3$ mTorr and (b) $P_{Ar}=8$ mTorr.

responding to sample $C8$ deposited at $P_{Ar}=8$ mTorr (Fig. 6). The presence of the (200) fcc line, and the decrease of (10$\bar{1}$0) and (10$\bar{1}$1) hcp lines indicates a more marked fcc character of sample $C3$ deposited at low $P_{Ar}=3$ mTorr.

IV. STRUCTURAL MODELS FOR AMORPHOUS $Co_{1-x}Ti_x$ THIN FILMS

A. Generalities — Available data in the literature

The formation of the amorphous state in $Co_{1-x}Ti_x$ thin films in the composition range investigated ($0.14 \leq x \leq 0.22$) can be attributed to the deep eutectic and the existence of the Co_3Ti intermetallic compound.[7] Actually no general structural model exists which permits us to describe the amorphous state. One way to represent the atomic arrangement of this state is the dense random packing of hard-sphere (DRPHS) models.[8] In its simplest form the a-$Co_{1-x}Ti_x$ is a binary alloy. Its structure can be represented by a random mixture of Co and Ti, where the Ti is in a substitutional position in the DRPHS because its atomic radius is of the same order of magnitude as that of the Co.

The structural studies reported in the literature were performed on rapidly quenched $TM_{1-x}M_x$ type metallic glass, rich in M, where TM is a late transition metal and M the glass-forming early transition metal.[9–20] No detailed study of TM-rich alloys exists. There are indications that the local environment is not as random as the DRPHS model predicts. Indeed the analysis of x-ray as well as neutron-diffraction spectra revealed that in amorphous $(Cu,Ni)_{1-x}(Ti,Zr)_x$ alloys a strong tendency exists toward the formation of a chemical short-range order (CSRO).[10,11,14,18,20] This result was also confirmed on these alloys by an EXAFS study.[12,15] In a-$Cu_{1-x}Zr_x$,[19] a-$Ni_{1-x}Zr_x$,[20] and a-$Cu_{1-x}Y_x$ (Ref. 21) it was found that the CSRO increases with increasing TM content. The similarity between the SRO in a-$Cu_{60}Zr_{40}$ and crystalline Cu_3Zr_2,[15] as well as between a-$Ni_{26}Ti_{74}$ and crystalline $NiTi_2$,[11] led us to propose the hypothesis of a chemical and structural short-range order. Our experimental results of a-$Co_{1-x}Ti_x$ films are quite similar to the structure factor corresponding to a-$Cu_{1-x}Ti_x$ (Ref. 10) and a-$Ni_{26}Ti_{74}$ (Ref. 11) which leads to the conclusion that a topological SRO exists in these films.

The interference function $i(s)$ for the two-sized particle DRP model was determined by Sadoc *et al.*[22] The as-computed $i(s)$ agrees with our experimental results on a-$Co_{86}Ti_{14}$ for atomic radii size ratio $\sigma=0.9$, and an amount of the small sphere size equal to 10 to 15%. However, the a-$Co_{86}Ti_{14}$ is formed by 86% of small spheres ($R_{Co}=1.26$ Å) and 14% of large ones ($R_{Ti}=1.45$ Å), with $\sigma=R_{Co}/R_{Ti}=0.869$. The main difficulty in this approach is to choose the value of the hard-sphere radius. Even though the as-computed density is close to the experimental value, a change by a small amount of the interatomic distance induces large variations in the density of the model.[23] In these conditions the agreement between the as-computed and experimental density is not a sufficient argument in favor of this model. Moreover, this model exhibits a long-range order which is much better defined than that observed experimentally.

An energetic relaxation of DRP models results in an increase of the atomic density, but the agreement is more or less good between the as-computed and experimental position and the shape of the as-split second halo. Boudreaux *et al.*[24] studied the effect of energetic relaxation on a two-sized sphere model. The radial distribution function (RDF) reproduces the main features of the experiments, but the shoulder on the second peak is not apparent on $i(s)$. Generally $i(s)$, as well as the RDF, depend upon the algorithm of packing[22,25–30] and upon the forms of the pair interaction potential[24,28,31–33] that are used. One obtains a unique interference function for a given algorithm and pair interaction potential. However, the experiments are not actually sufficiently precise in order to permit a choice of a single form of algorithm or potential. In these conditions it was impossible to reproduce the as-detected modifications of the TEDP's which we detected on films having the same Ti concentration but prepared under various pressures of the sputtering gas P_{Ar}. Finally the DRP model agrees with a short-range directional order, a mechanism which did not allow us to explain the variation of K_u with P_{Ar}.

All these results are in favor of the hypothesis that in Co-rich $Co_{1-x}Ti_x$ amorphous thin films a topological SRO exists which cannot be reproduced by a DRP of individual atoms. The topological SRO which is characteristic of an amorphous state can be determined by considering the available structural data obtained on the related crystalline compound.

On the Co-Ti phase diagram[7] three phases are observed for the concentration range $0 \leq x \leq 0.25$: β-Co having the fcc structure, which when decomposed gives

the α-Co of hcp structure and the intermetallic compound Co_3Ti.[34,35] The Co_3Ti posses either an ordered fcc structure isomorphic to $AuCu_3$ or the hexagonal structure of Ni_3Ti (Ref. 36), where octahedral and trigonal sites are intermixed. In pure crystalline Co the hcp phase is generally preponderant at room temperature, nevertheless in most cases both the hcp and fcc structures coexist in pure Co and Co-based crystalline alloys. These crystalline structures exhibit, respectively, the trigonal and octahedral local symmetries. On bulk crystalline samples the field-cooled induced magnetic anisotropy was attributed to the formation of a texture in the hcp phase but it could not be directly detected by x-ray diffraction.[37,38] Therefore the experimental difficulties are increased in a study of amorphous films by electron diffraction.

B. Construction of the theoretical structural model

According to the discussion reported in Sec. IV A if we assume that the amorphous $Co_{1-x}Ti_x$ retain the local symmetry of the crystalline counterpart, the structural model should contain sites having hcp- and fcc-like symmetries. Several authors developed structural models for amorphous alloys based upon packing of icosahedral clusters,[39–43] because the corresponding interference function $I(s)$ exhibits the main characteristics of the diffraction pattern of metallic glasses. So we considered the model as a random packing of three types of clusters: octahedral and trigonal clusters related, respectively, to the fcc and hcp crystalline structure and clusters having the icosahedral arrangement. Corb *et al.*[44] put forward a similar hypothesis in order to explain the magnetic hysteresis exhibited by CoBNb metallic glass but no structural model based upon this assumption was reported in the literature. Here we report the modeling process for samples of concentration $Co_{86}Ti_{14}$ (samples *C*) and indicate in the discussion how these results can be applied to films with higher Ti concentration.

$I(s)$ is given in electron units (e.u.) by the Debye scattering equation

$$I(s)_{\text{e.u.}}=\sum_i \sum_j f_i f_j \frac{\sin 2\pi s r_{ij}}{2\pi s r_{ij}} \tag{1}$$

for an array of N atoms which takes all orientations in space, r_{ij} is the distance of each $(\text{Co, Ti})_i$ atom from every other $(\text{Co,Ti})_j$ atom and f is the scattering factor. The interatomic distances r_{ij} were computed from $R_0=1.26$ Å. R_0 corresponds to the atomic radius of the mean (Co,Ti) atom and was deduced from "a"$=3.75$ Å related to an fcc solid solution β-Co containing 14 atomic percent of Ti.[36]

As the location of the Co and Ti atoms in the structure is actually unknown the scattered intensities $I(s)$ were computed by assuming that they are distributed randomly. Consequently, the structural model was constructed using the average atomic scattering factor f

$$f=(1-x)f_{\text{Co}}+xf_{\text{Ti}}\ , \tag{2}$$

where x is the Ti content and f_{Co} and f_{Ti} are the kinematic electron scattering factors of Co and Ti as given by Doyle *et al.*[45]

For an easier numerical analysis we used the dimensionless reduced interference function

$$i(s)=I(s)/Nf^2-1\ . \tag{3}$$

In the following, the various clusters are designated by (O/n), (T/n), and (I/n) where O, T, and I correspond

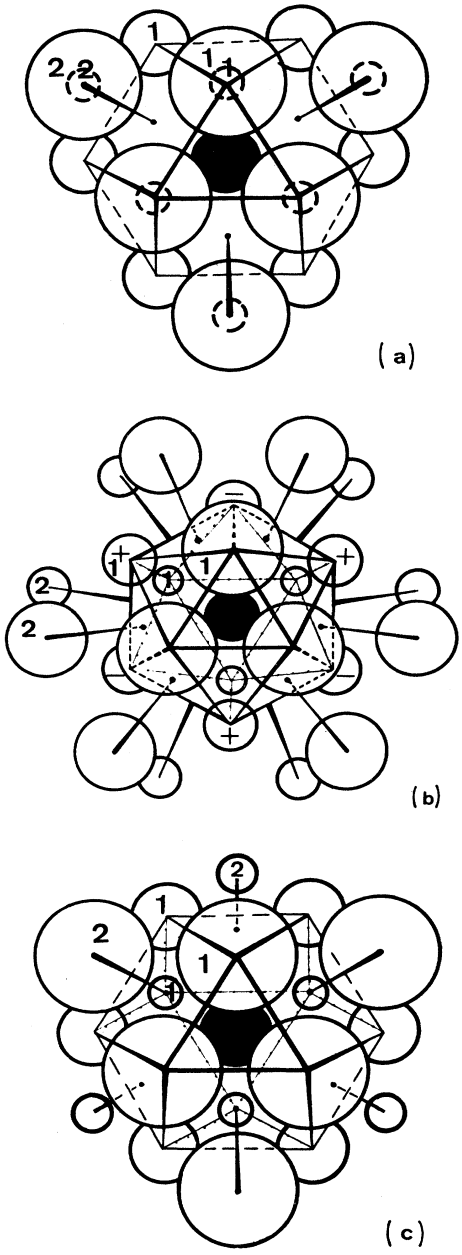

FIG. 7. Different clusters considered in the theoretical model. (a) Cluster of 19 atoms ($T/19$) on trigonal site, (b) cluster of 25 atoms ($I/25$) on icosahedral site, and (c) cluster of 19 atoms ($O/19$) on octahedral site. The projection plane is perpendicular to a threefold A_3 axis. The circles numbered (1) and (2) are, respectively, the nearest- and second-nearest neighbor atoms of the central atom represented by a full circle.

to clusters with octahedral, trigonal, and icosahedral symmetry and n the number of atoms forming up the clusters. Here $n=13$, 19, 25, or 33. $(O/13)$, $(T/13)$, and $(I/13)$ correspond to the basic clusters of 12 atoms around a central particle and having the indicated symmetry. $(O/19)$ and $(T/19)$ are formed, respectively, of the basic unit $(O/13)$ and $(T/13)$ which are surrounded by six second-neighbor atoms with the same configuration as in the fcc and hcp structure [Figs. 7(a) and 7(c)]. By placing an additional atom on each of the 20 triangular faces of the $(I/13)$ cluster, the resulting unit is the $(I/33)$ dodecahedral cluster. The $(I/25)$ cluster [(Fig. 7(b)] contains 12 of the 20 second-neighbor atoms of the dodecadron $(I/33)$.

In a first step we considered the model as a $(O/13)_{1-\alpha}(T/13)_{\alpha}$ alloy, where α is the fraction of $(T/13)$ unit; hence the local configuration reproduces the symmetry of the crystallographic structure of α-Co, β-Co, or Co_3Ti.

The reduced interference functions $i(s)$ related to the $(T/13)$ or $(O/13)$ units are reported on Figs. 8(a1) and 8(b1). The right asymmetry of the second maximum is obtained by close packing the $(T/13)$ or the $(O/13)$ clusters with a hexagonal two-dimensional layer formed by seven atoms [called hereafter $(H\text{-}L\text{-}7)$]. This $(H\text{-}L\text{-}7)$ layer is perpendicular to the threefold symmetry axis A_3 of the as-joined clusters [Figs. 8(a2) and 8(b2)].

In order to reproduce the high atomic density of amorphous alloys there exists two ways of packing the random continuous lattice $(O/13)_{1-\alpha}(T/13)_{\alpha}$. The two nearest-neighbor clusters possess a common triangular face, or linked by the $(H\text{-}L\text{-}7)$ hexagonal layer, so that, for instance, an infinite random chain of $(O/13)_{0.5}(T/13)_{0.5}$ may be built up. In the first case the shoulder of the second peak of $i(s)$ is barely resolved. With the second linkage the maximum shifts slightly towards lower values of s ($s=0.87$ Å) but this value is still too high and the splitting of the second peak appears too accentuated [(Figs. 8(c) and 8(d)].

In a second step we included the $(I/13)$ clusters in the model which consist now of an infinite random chain $(T/13)_{1/3}(O/13)_{1/3}(I/13)_{1/3}$, where two $(I/13)$ clusters as nearest neighbors are excluded. The as-computed $i(s)$ reproduce the experimental curve more faithfully, however, the profile of the first peak disagrees because the size of the clusters are too small [Fig. 8(e)].

At this step of modeling we can deduce from the previous studies the following basic principles for further computations: (i) the various clusters are packed in a way that cannot be related to any known crystalline structure, (ii) two (T/n) or (O/n) clusters [or (T/n) and (T/n), or (O/n) and (O/n)] having a common A_3 axis are correlated by a $(H\text{-}L\text{-}7)$ layer. (iii) The size of the various clusters must be kept smaller than the size of the largest discernable detail deduced from the TEM (≈ 10 Å), but have to be adjusted in order to improve the first peak profile of $i(s)$ without modifying the second one. In the following we considered the structure formed by

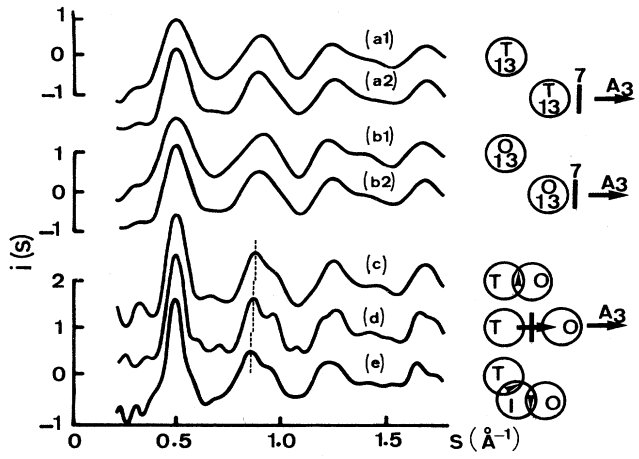

FIG. 8. Computed reduced interference functions $i(s)$ corresponding to various atomic configurations. (a1) Trigonal cluster of 13 atoms $(T/13)$, (b1) octahedral cluster of 13 atoms $(O/13)$, (a2) close-packing of a $(T/13)$ unit with a hexagonal two-dimensional layer of 7 atoms $(H\text{-}L\text{-}7)$ along a threefold A_3 axis. (b2) Close-packing of a $(O/13)$ unit with a $(H\text{-}L\text{-}7)$. (c) Infinite random chain $(T/13)_{o.5}(O/12)_{o.5}$ where two nearest-neighbor clusters possess a common triangular face. (d) Infinite random chain $(T/13)_{o.5}(O/13)_{o_o.5}$ where two nearest-neighbor clusters are linked by a $(H\text{-}L\text{-}7)$. (e) Infinite random chain $(T/13)_{1/3}(O/13)_{1/3}(I/13)_{1/3}$ which excludes two $(I/13)$ clusters as nearest neighbors.

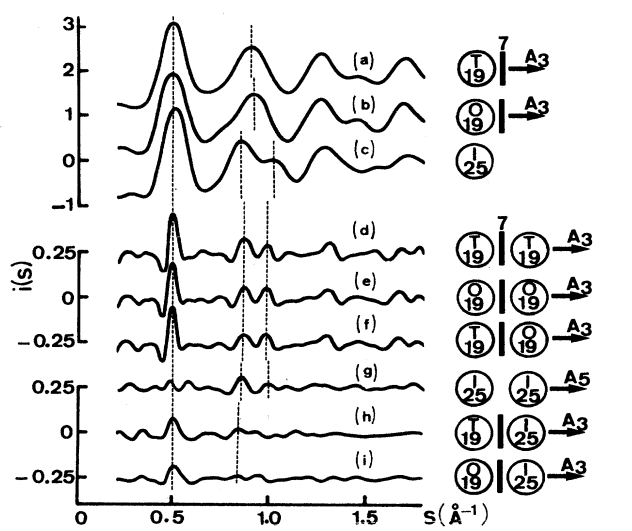

FIG. 9. Computed $i(s)$ corresponding to various clusters: (a) Close-packing of a $(T/19)$ cluster with a $(H\text{-}L\text{-}7)$. (b) Close-packing of a $(O/19)$ cluster with $(H\text{-}L\text{-}7)$. (c) $(I/25)$ cluster. Computed correlation functions between nearest-neighbor clusters along a threefold A_3 axis. The atomic units are linked by a $(H\text{-}L\text{-}7)$ layer. (d) $(T/19)$-$(T/19)$ correlations; (e) $(O/19)$-$(O/19)$ correlation; (f) $(T/19)$-$(O/19)$ correlations; (h) $(T/19)$-$(I/25)$ correlations; (i) $(O/19)$-$(I/25)$ correlations. (g) Correlation along a five-fold A_5 axis: $(I/25)$-$(I/25)$.

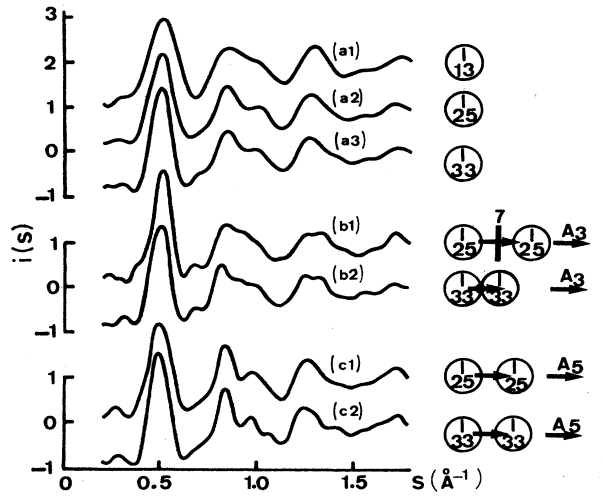

FIG. 10. Computed $i(s)$ related to clusters on icosahedral site and assemblies of such clusters. (a1) Icosahedral $(I/13)$ cluster of 13 atoms, (a2) $(I/25)$ cluster of 25 atoms, (a3) dodecahedral $(I/33)$ cluster of 33 atoms. Infinite random chains of clusters (I) where two joined units possess the following: (b1), (b2) a common three-fold A_3 axis; (c1), (c2) a common five-fold A_5 axis, (b1), (c1) assembly of $(I/25)$ clusters, and (b2), (c2) assembly of $(I/33)$ clusters.

$(T/19)_{1-\alpha-\beta}(O/19)_\alpha(I/n)_\beta$ clusters with $n=25$ or 33. (iv) The respective amount and the correlation between the various clusters have to be adjusted by comparing the as-computed spectra with the experimental data.

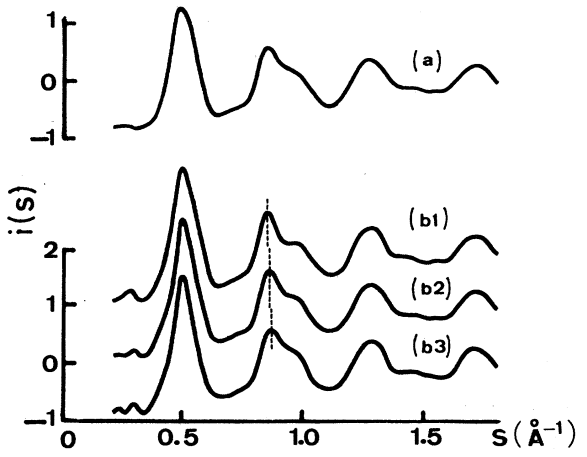

FIG. 11. Theoretical amorphous alloy $(T/19)_{1-\beta}(O/19)_0(I/25)_\beta$ as a rancom continuous chain of $(T/19)$ and $(I/25)$ units. Computed $i(s)$ for various values of β and various contributions of correlations between the atomic units. (a) $\beta=0.5$, no $(T/19)$-$(T/19)$ correlations, 50% of $(T/19)$-$(I/25)$ correlations, 50% of $(I/25)$-$(I/25)$ correlations. (b1) $\beta=2/3$, 14% of $(T/19)$-$(T/19)$, 29% of $(T/19)$-$(I/25)$, 57% of $(I/25)$-$(I/25)$, (b2) $\beta=1/2$, 20% of $(T/19)$-$(T/19)$, 40% of $(T/19)$-$(I/25)$, 40% of $(I/25)$-$(I/25)$, (b3) $\beta=1/3$, 33% of $(T/19)$-$(T/19)$, 33% of $(T/19)$-$(I/25)$, 33% of $(I/25)$-$(I/25)$.

The as-computed $i(s)$ corresponding to $(O/19)$ or $(T/19)$ close-packed with a $(H\text{-}L\text{-}7)$ layer are reported on Figs. 9(a) and 9(b). The two reduced interference functions have practically the same shape. The size and the accurate correlations of the (I/n) icosahedral clusters were deduced from Figs. 10(a1)–10(c2) by comparing them with the experimental data. Following Figs. 10(a2)–10(a3) and Figs. 10(c1)–10(c2) a better agreement is obtained for an array of $(I/25)$ than for a $(I/33)$ one. The correlation of two joint (I/n) clusters have to be along a common fivefold axis A_5 rather than along a common A_3 one [Fig. 10(c1)]. Finally the configuration corresponding to the $(I/25)$ cluster also permits a close packing with an $(O/19)$ or $(T/19)$ cluster along a common A_3 axis while this is not possible for a $(I/33)$ cluster.

To sum up, the best agreement with the experimental diffraction spectra is obtained when structural model is built up of $(T/19)$, $(O/19)$, and $(I/25)$ units. We introduced angular correlations so that the various clusters are surrounded by preferentially oriented units. The allowed correlations are reported in Figs. 9(d)–9(i).

The analysis of these correlation functions revealed that if one takes into account the contribution of the correlations $(O/19)$-$(O/19)$, $(T/19)$-$(T/19)$, or $(O/19)$-$(T/19)$, the width of the first maximum and the contrast of the splitting of the second one can be improved on $i(s)$. These effects are illustrated on $i(s)$ which was computed for the model $(O/19)_0(T/19)_{0.5}(I/25)_{0.5}$. In a first

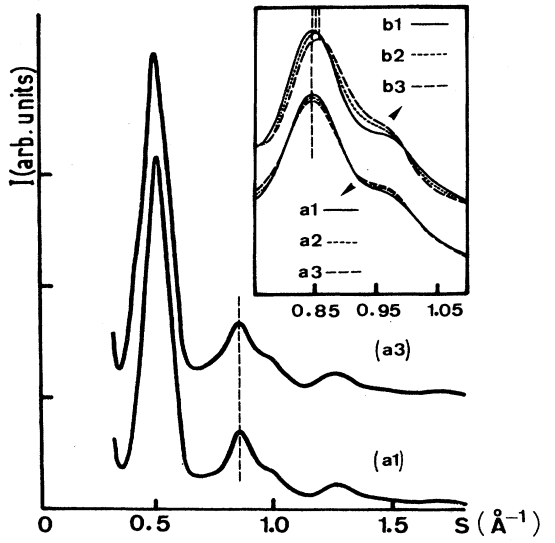

FIG. 12. Theoretical intensities $I(s)$ diffused by a random continuous chain of $(T/19)_{1-\alpha-\beta}(O/19)_\alpha(I/25)_\beta$. Illustration of the effect of clusters $(O/19)$ as substitute units for clusters $(T/19)$. The amount of $(I/25)$ clusters remains constant with $\beta=\frac{2}{3}$. (a1) $\alpha=0$; (a2) $\alpha=\frac{1}{6}$; (a3) $\alpha=\frac{1}{3}$. In the inset: The as-computed profile of the second maximum of $I(s)$ as a function of the amount of $(I/25)$ clusters. (b1) $\alpha=0$, $\beta=2/3$; (b2) $\alpha=0$, $\beta=1/2$; (b3) $\alpha=0$, $\beta=\frac{1}{3}$. The corresponding interference functions $i(s)$ are shown in Figs. 11(b1)–11(b3).

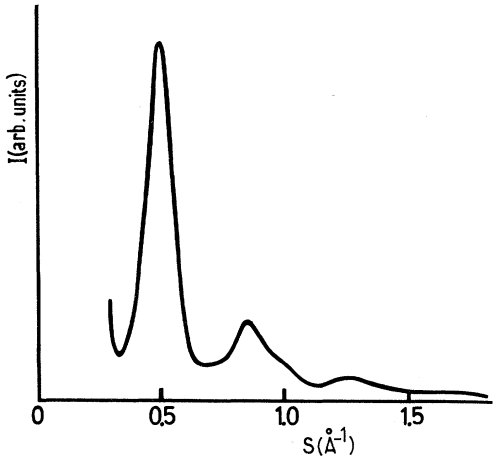

FIG. 13. Theoretical intensities $I(s)$ computed for the continuous chain $(T/19)_{1/3}(O/19)_o(I/25)_{2/3}$ by replacing each sphere of atomic coordination r_{ij} by a Gaussian distribution with a variance $0.03r_{ij}$.

case two nearest-neighbor $(T/19)$ clusters were excluded [Fig. 11(a)]. In the second one the contribution of the various correlations were the following: 20% of $(T/19)$-$(T/19)$, 40% of $(T/19)$-$(I/25)$, and 40% of $(I/25)$-$(I/25)$ [Fig. 11(b2)]. The best agreement with experiment was obtained when we took into account the correlation $(T/19)$-$(T/19)$.

Finally we tried to simulate the slight variations of the experimental TEDP (Fig. 3) as a function of P_{Ar} by changing the respective amount of the various clusters, in the as-proposed model $(T/19)_{1-\alpha-\beta}(0/19)_\alpha(I/25)_\beta$. If one keeps the amount of $(I/25)$ clusters constant (β=constant) and one changes the respective fraction of $(T/19)$ and $(O/19)$ clusters, its effect upon the characteristics of the as-computed $I(s)$ is negligible [Figs. 12(a1)–12(a3)]. This result was expected from the similarity between the various reduced interference functions $i(s)$ of Figs. 9(a) and 9(b), the correlation function of Figs. 9(d)–9(f) on the one side and that of Figs. 9(h)–9(i) on the other.

Consequently, the model does not permit us to distinguish between the octahedral and trigonal units. However, $x=0.14$ is the lowest concentration in Ti for which one obtains an amorphous phase for $P_{Ar}=8$ mTorr so the probability is high to find in the deposit fcc- and hcp-like sites, both of which exist in Co-rich crystalline alloys. In these conditions the respective evolution of octahedral and trigonal clusters with P_{Ar} was deduced from the magnetic properties as reported in paper I.

By contrast a significant change in the feature of $I(s)$ is observed if one increases progressively the amount of $(I/25)$ clusters with respect to $(O/19)$ and/or $(T/19)$ ones. As illustrated in Figs. 11(b1)–11(b3) and Figs. 12(b1)–12(b3) the second maximum shifts towards lower values of s, and the shoulder of the second peak becomes more marked.

In films where the Ti concentration was higher we observed an attenuation of the shoulder on the second peak. We believe that the various clusters, in particular, the trigonal and octahedral ones, are progressively deformed when the Ti content in the film is increased. This more disordered local structure can be simulated in the as-computed $I(s)$ by replacing each sphere of atomic coordination r_{ij} by a Gaussian distribution with a variance of σr_{ij}. For $\sigma=0.03$ no overlaps exist between nearest-neighbor atoms and one can reproduce simultaneously the more attenuated shoulder of the second peak and the damping of the oscillations (Fig. 13).

V. DISCUSSION AND CONCLUSIONS

The position and the profile of the experimental intensities $I(s)$ scattered by the amorphous samples C ($Co_{86}Ti_{14}$) as obtained at various pressures of the sputtering gas P_{Ar} can be well reproduced by assuming as an amorphous model a random continuous network of octahedral $(O/19)$, trigonal $(T/19)$, and icosahedral $(I/25)$ clusters. The variations of K_u as a function of the pressure of the sputtering gas P_{Ar} was explained, using the present structural model, by assuming a structural transformation in the amorphous state that involves a small distortion of a fraction of the icosahedral clusters which takes at low and high P_{Ar}, respectively, an octahedral and trigonal configuration. Films obtained at the lowest pressure ($P_{Ar}=3$ mTorr) are built up of icosahedral and low-anisotropy octahedral clusters, a result which explains that, for this pressure, K_u is minimal. In films prepared at high P_{Ar} (15 mTorr), a significant amount of trigonal clusters are developed, a result which explains that K_u is much higher than for 3 mTorr but more or less oriented randomly. When $P_{Ar}=8$ mTorr the energy of the particles is closed to the activation energy for which the phase transformation is the largest.[44] During the cooling, some of the icosahedral clusters are transformed to trigonal ones and these clusters will be oriented along the applied field in order to minimize the total energy acting on the film. The amount of icosahedral clusters is the largest for $P_{Ar}=8$ mTorr, i.e., when K_u is maximum. This effect is revealed on experimental and theoretical $I(s)$ by a shift of the second maximum towards lower values of s and a more marked shoulder on the second peak.

In conclusion a new structural model was established for amorphous CoTi thin films deposited by rf sputtering and permitted to explain both magnetic and structural experimental results. The main hypothesis, that the structure is built up of clusters which have a configuration similar to that of the corresponding crystalline compound, was based upon the magnetic properties. The existence of these clusters was proved in a formal way by the thermomagnetic annealing experiences as reported in paper I. Careful scattering measurements permitted us to detect slight but significant changes of the structural properties as a function of P_{Ar} and concentration. These structural changes were explained by the present model, which also permitted us to understand the related variations of the induced anisotropy K_u.

ACKNOWLEDGMENTS

The authors acknowledge J. Sztern for high-quality technical assistance.

*Also at Laboratoire de Science et Génie des Materiaux Metalliques, Parc de Saurupt, 54042 Nancy CEDEX, France.
†Present address: IBM Almaden Research Center, San Jose, California.

[1]K. Ounadjela, Ph.D. thesis, Université de Paris, VII, 1986 (unpublished).
[2]G. Suran, K. Ounadjela, and F. Machizaud, Phys. Rev. Lett. **57**, 3109 (1986).
[3]J. C. Slonczewski, J. Appl. Phys. **29**, 448 (1958).
[4]L. Neel, C. R. Acad. Sci. **237**, 1613 (1954); **238**, 305 (1954).
[5]T. Iwata, Sci. Rep. Res. Inst. Tohoku Univ. **13**, 356 (1961).
[6]A. Naudon and A. M. Flank, in *Proceedings of the Fourth International Conference on Rapidly Quenched Metals,* edited by T. Masumoto and K. Suzuki (Japan Inst. of Metals, Sendai, 1982), p. 425.
[7]J. L. Murray, Bull. Alloy Phase diagrams **3**, 74 (1982).
[8]J. D. Bernal, Nature (London) **185**, 68 (1960); J. D. Bernal, Proc. R. Soc. London, Ser. A **280**, 299 (1964).
[9]Y. Waseda, *The Structure of Non-Crystalline Materials* (McGraw-Hill, New York, 1980).
[10]M. Sakata, N. Cowlam, and H. A. Davies, in Ref. 6, p. 327.
[11]T. Fukunaga, K. Kai, M. Naka, N. Watanabe, and K. Susuki, in Ref. 6, p. 347.
[12]D. Raoux, J. F. Sadoc, P. Lagarde, A. Sadoc, and A. Fontaine, J. Phys. **8**, C8-207 (1980).
[13]M. Sakata, N. Cowlam, and H. A. Davies, J. Phys. F **11**, L157 (1981).
[14]C. N. J. Wagner and D. Lee, J. Phys. **41**, C8-242 (1980).
[15]A. Sadoc, D. Raoux, P. Lagarde, and A. Fontaine, J. Non-Cryst. Solids **50**, 331 (1982).
[16]T. Mizoguchi, T. Kudo, and T. Irishwa, in *Proceedings of the Third International Conference on Rapidly Quenched Metals,* edited by B. Cantor (The Metal Society, London, 1978), p. 384.
[17]R. Haensel, P. Rabe, G. Tolkiehm, and A. Werner, in *Liquids and Amorphous Metals,* Vol. 467 of *NATO Advanced Study, Series B: Physics,* edited by E. Lucher and X. Coufal (Plenum, New York, 1980), p. 467.
[18]J. F. Sadoc, H. J. Güntherodt, and C. N. J. Wagner, *Glassy Metals II,* edited by X. Beck, (Springer, Berlin, 1983), p. 51.
[19]W. Sperl, P. Lamparter, S. Streeb, and S. Cummings, Ann. Rep. I.L.L. 183 (1981).
[20]D. Lee, A. Lee. C. N. J. Wagner, L. E. Tanner, and A. K. Soper, J. Phys. **43**, C9-19 (1982).
[21]A. M. Flank, Ph.D. thesis Université de Poitiers 1983 (unpublished).
[22]J. F. Sadoc, J. Dixmier, and A. Guinier, J. Non-Cryst. Solids **12**, 46 (1973).
[23]D. S. Boudreaux and H. J. Frost, Phys. Rev. B **23**, 1506 (1981).
[24]D. S. Boudreaux and J. M. Gregor, J. Appl. Phys. **48**, 152 (1977); **48**, 5057 (1977).
[25]J. L. Finney, Proc. R. Soc. London, Ser. A **319**, 479 (1970).
[26]C. H. Bennett, J. Appl. Phys. **43**, 2727 (1972).
[27]A. J. Matheson, J. Phys. C **7**, 2569 (1974).
[28]J. A. Barker, M. R. Hoare, and J. L. Finney, Nature (London) **257**, 120 (1975).
[29]T. Ichikawa, Phys. Status Solidi A **29**, 293 (1975).
[30]J. Bletry, Z. Naturforsch. Teil A: **32**, 445 (1977).
[31]L. von Heimendall, J. Phys. F **5**, L141 (1975).
[32]J. L. Finney, Mater. Sci. Eng. **23**, 199 (1976).
[33]C. H. Bennett and J. L. Finney, *Rapidly Quenched Metals* (MIT, Cambridge, Massachusetts, 1976), p. 231.
[34]H. Bribring and J. Manene, C. R. Acad. Sci. **249**, 1508 (1959).
[35]R. W. Fountain, G. M. Faubring, and W. D. Forgeng, Trans. AIME **221**, 747 (1961).
[36]W. B. Pearson, *A Handbook of Lattice Spacings and Structures of Metals and Alloys* (Pergamon, Oxford, 1967), Vol. 2, p. 816.
[37]M. Takahashi, J. Phys. Soc. Jpn. **47**, 1110 (1979).
[38]C. D. Graham, Jr., J. Phys. Soc. Jpn. **17**, 321 (1962).
[39]J. Farges, B. Raoult, and G. Torchet, J. Chem. Phys. **59**, 3454 (1973).
[40]C. L. Briant and J. J. Burton, Phys. Status Solidi B **85**, 393 (1978).
[41]F. Machizaud, F. A. Kuhnast, and J. Flechon, Ann. Chim. (Paris) **3**, 177 (1981).
[42]D. S. Boudreaux and H. F. Frost, Phys. Rev. B **23**, 1506 (1981).
[43]P. J. Steinhardt, D. R. Nelson, and M. Ronchetti, Phys. Rev. Lett. **47**, 1297 (1981).
[44]B. W. Corb, R. C. O'Handley, J. Megusar, and N. J. Grant, Phys. Rev. Lett. **51**, 1386 (1983).
[45]P. A. Doyle and P. S. Turner, Acta Crystallogr. A **24**, 390 (1968).

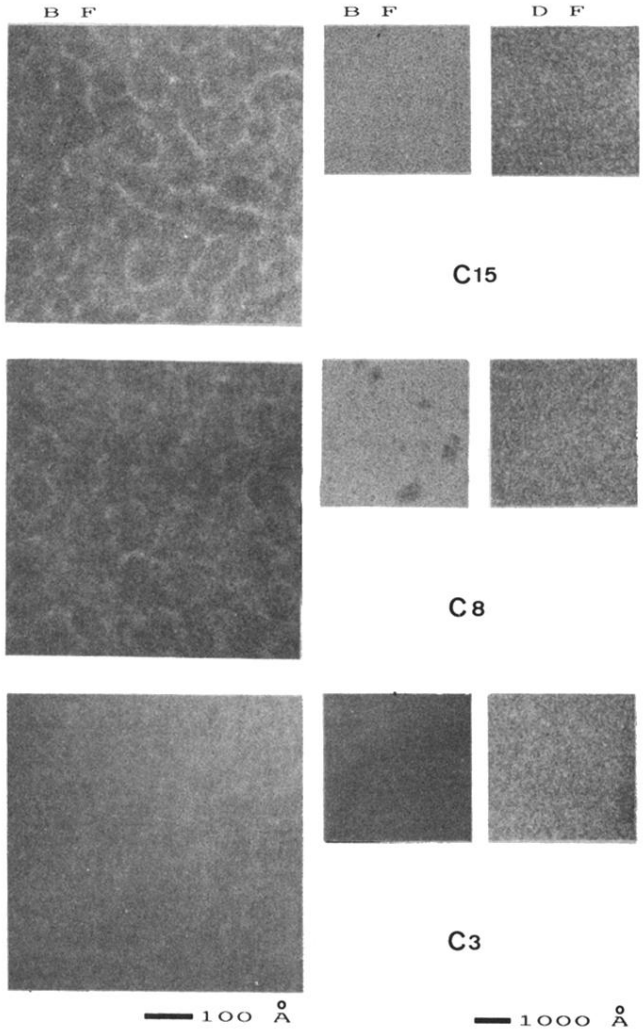

FIG. 1. Microstructure of $Co_{86}Ti_{14}$ thin films in bright field (BF) and dark field (DF) and evolution with P_{Ar}. Samples *C*3, *C*8, and *C*15 were deposited, respectively, at 3, 8, and 15 mTorr.

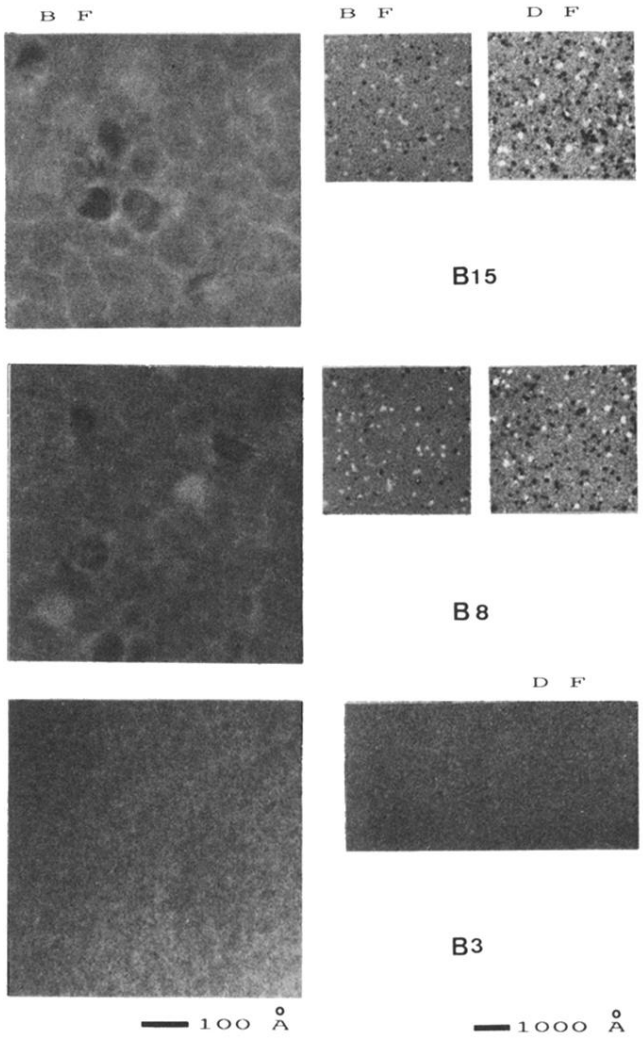

FIG. 2. Microstructure of $Co_{88}Ti_{12}$ thin films in BF and DF samples *B*3, *B*8, and *B*15 were deposited, respectively, at $P_{Ar}=3$, 8, and 15 mTorr.